Corresponding author contact: Grace Shephard - grace.shephard@geo.uio.no

Seismological Expression of the Iron Spin Crossover in Ferropericlase in the Earth's Lower Mantle

Grace E. Shephard*[1], Christine Houser[2], John W. Hernlund[2], Juan J. Valencia-Cardona[3],Reidar G.

Trønnes[1,4], Renata M. Wentzcovitch[2,5,6]

[1]*Center for Earth Evolution and Dynamics (CEED), Department of Geosciences, University of

Oslo, Norway*

[2]*Earth-Life Science Institute, Tokyo Institute of Technology, Tokyo, Japan*

[3]*Department of Chemical Engineering and Material Science, University of Minnesota, Twin Cities,

USA*

[4]*Natural History Museum, University of Oslo, Norway*

[5]*Department of Earth and Environmental Sciences, Columbia University, Lamont-Doherty Earth

Observatory, Palisades, USA*

[6]*Department of Applied Physics and Applied Mathematics, Columbia University, New York City,

USA*

1 **The two most abundant minerals on Earth which together make up over 90% of the Earth's**

2 **lower mantle are (Mg,Fe)O-ferropericlase (Fp) and $(Mg,Fe)SiO_3$-bridgmanite (Bm). Iron in**

3 **Fp undergoes a high-spin to low-spin (HS-LS) crossover that influences density, viscosity,**

4 **elasticity, thermal conductivity, and elemental partitioning[1–4], however, the predicted effects**

5 **of this transition are not apparent in global 1D seismic velocity profiles[5]. This discrepancy**

6 **suggests that the predictions are inaccurate, seismic resolution is insufficient to resolve the**

effects, or a substantial portion of the mid-lower mantle is relatively SiO_2-rich (hence Fp-poor) compared to the shallow mantle. The melt-depleted mantle lithosphere of subducted oceanic slabs that sink into the lower mantle contains ~22% Fp[6], and thus offers the best opportunity to prospect for a spin change in Fp. Here we reveal a loss in the abundance of fast seismic velocity anomalies in compressional (P-wave) tomography models at ~1,400-2,000 km depth that is opposite to the trend in shear (S-wave) models. This can be explained by the decreasing temperature sensitivity of P-velocity expected for the mixed spin state of iron in Fp at corresponding pressures[7]. We also observe a similar but subtle signal for seismically slow regions below ~1,800 km, consistent with a pressure increase and broadening of the Fp spin transition at higher temperatures[4,8]. Seismic wave raypath distribution is similar for both P- and S-waves in this depth range[9], therefore this signature cannot be attributed to substantial differences in data coverage. Our identification of the spin transition signal in seismically fast and slow regions indicates that the spin crossover can identify the presence of Fp in the lower mantle. The absence of a Fp spin crossover signal in global seismic profiles supports the notion that the lower mantle is chemically heterogeneous at large scales and contains SiO_2-rich regions that suppress the average signature of these pressure-induced electron spin-pairing transitions.

The rocky silicate Earth is volumetrically dominated by the lower mantle, but its major element abundance remains elusive. Unambiguous seismic detection of a spin crossover in Fp would yield an important constraint on lower mantle composition. Advances in mineral physics[1–3,10,11] consistently predict that Fe^{2+} in Fp undergoes a HS-LS crossover at mid-lower mantle conditions

(Fig. 1a), and its distinct effects on seismic wavespeeds offer a clear target for geophysical detection (Fig. 2). In particular, a volume reduction during the spin crossover[2] inevitably causes a decrease of the bulk modulus in the mixed spin region[4,8,12,13]. The temperature dependence of the pressure onset and pressure range of the HS-LS crossover results in an anomalous dependence of the bulk modulus on temperature with little influence on the shear modulus (Fig. 2a). The magnitude of this effect increases for higher iron contents and modal abundance of Fp. For our calculations assuming 17% Fp with 15 mol% of FeO, shear (S-wave) velocities (Fig. 2b) retain temperature sensitivity while longitudinal (P-wave) velocities (Fig. 2c) become less sensitive to temperature variations[7] during the spin crossover. Thus, temperature anomalies in Fp-bearing rock have a distinctive seismic signal: S-wave anomalies persist but P-wave anomalies weaken within the mixed spin region.

In the lower mantle, the deep extension of cold and sinking subducted oceanic lithosphere (which contains $\sim$22% Fp[6]) is usually identified via fast seismic anomalies[14,15]. Thus, we isolate patterns within fast wavespeed anomalies in P-wave and S-wave models to examine whether a crossover signal is present. In spite of similar P- and S-wave coverage and thus similar resolution in the mid-lower mantle[9,16], distinctly different patterns emerge when comparing fast variations between P- and S-wave tomography models[17,18]. In particular, for individual tomography model pairs such as HMSL[19](Extended Data. Figs. 1-3) the area covered by fast seismic anomalies at lower mantle depths reveals a mid lower-mantle drop in the abundance of P-wave anomalies relative to S-wave anomalies.

While these distinct patterns in particular P-wave and S-wave anomaly abundance profiles appear in a number of model comparisons (Extended Data. Figs. 1-3), we are cautious to interpret these as robust signals as each model utilizes different kinds of input data, parameterization, regularization, and other subjective choices in their construction. In particular, signals may appear that are artifacts of the particular tomographic input data and inversion approach rather than a genuine signal present in the lower mantle. However, we expect that the large degree of heterogeneity in tomographic data and modeling approaches will not consistently produce the same artifacts between all models, and therefore we employ a method that aims to cull the odd features of models while revealing only those characteristics that are reflective of a broad consensus of models [20]. For the signal we are seeking, artifacts are not not likely to consistently appear across all of the models.

We surveyed a suite of four P-wave and four S-wave tomography models (see Methods; a graphical explanation is provided in Extended Data. Fig. 4). The highest count (Fig. 1b-c) means that all for models agree in terms of fast anomalies at a given depth within the Earth. Importantly, this procedure does not add any features not already present in the constituent tomography models, but rather strip away potentially anomalous features that are particular to individual models. We first examine patterns in specific regions where the models consistently resolve a fast anomaly. As performed for the individual models, we separate the P- and S-wave signals for fast regions, which are now common to multiple tomography models in Fig. 1b-c. The models used to obtain the maps are detailed in the methods section and Extended Data. Figs. 1-4. The fast anomalies (Fig. 1b), reveal a distinct loss of fast P-wave anomalies relative to fast S-wave anomalies beginning ∼1,400 km depth. The observed depth range is similar to that predicted for the HS-LS crossover (the mixed

4

₆₉ spin region) in Fp (Fig. 1a).

₇₀   To further test the hypothesis that the decoupling in abundance of P-wave and S-wave anoma-

₇₁ lies reflects a spin crossover in Fp, we also seek a similar signature in seismically slow portions

₇₂ of tomographic models at greater depths, consistent with mineral physics predictions. Indeed, we

₇₃ find that the area coverage of slow anomalies (Fig. 1c) reveals the expected deeper departure (i.e.

₇₄ below $\sim$1800 km) in the abundance of slow P-wave anomalies relative to slow S-wave anomalies,

₇₅ consistent with a deepening of the spin transition at higher temperatures (Fig. 1a). While this slow

₇₆ signal is more subtle than the shallower decoupling between fast P- and S-wave anomalies, it adds

₇₇ strength to our interpretation that these consensus features of a variety of tomography models are

₇₈ likely due to the spin crossover, and reduce the likelihood that all of these signals are artifacts that

₇₉ are consistently reproduced across every type of tomographic modelling method that is represented

₈₀ in this suite of comparisons.

₈₁   Figs. 3-4 show the maps and cross-sections (respectively) of coherent structure for fast and

₈₂ slow anomalies. The P-wave anomalies are muted compared to S-wave anomalies in the mid

₈₃ mantle for both fast and slow anomalies (Fig. 4). For example, while fast anomalies attributed

₈₄ to subducted lithosphere appear contiguous through the mid-mantle in S-wave maps, the P-wave

₈₅ maps show coherent subducted lithosphere at the top and bottom of the lower mantle with a gap

₈₆ or weakening of the fast seismic signal in the mid mantle. Extended Data Fig. 5 shows difference

₈₇ maps, highlighting the spatial and depth-dependent differences between the P- and S-wave maps.

₈₈   We note that the abundance of fast P-wave and S-wave anomalies (Fig. 1b) increases below

5

89 ~2,500 km depth, with S-waves anomalies growing more rapidly toward the base of the mantle.

90 We speculate that the subtle relative difference between fast S- and P-anomalies near the core-

91 mantle boundary may be due to the appearance of post-perovskite in cold mantle, which is expected

92 to increase S-wave velocity by ~1-2% but has little effect on P-waves[21–23]. A drop in slow P-waves

93 relative to slow S-wave anomalies at the base of the mantle (~2,700 km Fig. 1c) is attributed to the

94 large low shear velocity provinces (LLSVPs) beneath the Pacific and Africa, and the divergence

95 in S- and P-wave behaviours has been used to argue for the presence of dense chemically distinct

96 piles in these regions[24].

97   The spin crossover is expected to influence the iron partitioning (K_D) between Bm and Fp[1,25]

98 by increasing the mol% of FeO in Fp, thus decreasing K_D[25]. Since the spin crossover may shift

99 to higher pressures as K_D decreases[4], the pressure range over which the crossover occurs could be

100 wider than that predicted for the constant partitioning value (K_D=0.5) we assign in our calculations.

101 We calculate the effect of depth-dependent K_D[25] on our predictions for the onset and depth range

102 of the spin crossover effect on P- and S-velocities (Extended Data. Fig. 7). The velocities with

103 variable K_D are barely distinguishable from the constant K_D case due to a very weak dependence

104 on the crossover depth to FeO content below 25 mol% (e.g.[26]). This prediction is consistent with

105 our observation that the effects of the crossover on P-velocities in fast velocity regions ceases by

106 ~2500 km depth (Fig. 1b).

107   While the mid-lower mantle drop in P-wave compared to S-wave anomalies is consistent

108 with the predictions of a spin crossover, it is difficult to reconcile with the ubiquitous presence

6

of Fp in the entire lower mantle. Despite seismic evidence for subduction of oceanic lithosphere into the deep mantle[27] and extensive mixing predicted by simple fluid-like models of whole mantle convection[28], we do not observe a decrease in P-velocity relative to S-velocity in globally averaged profiles (PREM; Fig. 1d). One possibility is that the offset of the spin transition at different temperatures prevailing at each depth mutes the global signature. However, it has previously been shown[29] that combined averages predicted for hot, average, and cool mantle geotherms still exhibit a characteristic inflection in P-wavespeed profiles even when accounting for the spin crossover in Fp. Another possibility is that the ambient mid-mantle is SiO_2-enriched compared to peridotitic material that circulates between the shallow and deep mantle, and a corresponding depletion of Fp in average mid-mantle domains effectively suppresses the globally averaged signature of the spin crossover[29].

1   Methods

Predictions of the Spin Crossover in Fp. Fig. 1a was calculated for $Mg_{1-x}Fe_xO$ with x=18.75% using published models[3,7]. The low spin fraction is calculated as:

$$n(P,T) = \frac{1}{1 + m(2S+1)\exp\left[\frac{\Delta G_{HS-LS}^{st+vib}}{X_{Fe}k_B T}\right]} \tag{1}$$

where $m = 3$ for the three possible orientations of minority electron d orbital (xy, yz, or zx) and S = 2. $\Delta G_{HS-LS}^{st+vib}$ includes only static and vibrational energy, without electronic entropy. Our elastic moduli and densities are also taken from published models[3,30–32]. These calculations used the rotationally invariant local density approximation LDA+U_{SC} method calculated with a self-consistent

7

127 Hubbard U[33]. Results for Fp were obtained using a 64-atom supercell with an iron concentra-

128 tion of x=18.75% (24 Mg, 32 O, and 6 Fe maximally separated from each other). Thermoelastic

129 properties were then obtained for other concentrations by linearly interpolating between x=0 and

130 x=18.75%. The vibrational density of states (VDOS) was computed using the vibrational virtual-

131 crystal model[8], and then used in conjunction with the quasiharmonic approximation to predict high

132 temperature effects. The magnitude of the predicted effects are in good agreement with experimen-

133 tal measurements[13]. Thermoelastic properties from[31,32] are used for Fe^{2+}-, Fe^{3+}- and Al-bearing

134 bridgmanite.

135   The shear and bulk modulus (Fig. 2a), S-wave (Fig. 2b) and P-wave velocity (Fig. 1d, 2c) are

136 calculated for a pyrolite[34] composition. The self consistent geotherms are calculated by setting the

137 starting temperature of the calculation at the top of the lower mantle to 1373 K (the -500 K case),

138 1873 (the average case), and 2373 K (the +500 K case) (see Extended Data. Fig. 6). The oxide

139 components are 45 wt.% SiO_2, 38 wt.% MgO, 8 wt.% FeO, 4 wt.% CaO, and 4 wt.% Al_2O_3, and the

140 rock mineralogy is 76 wt.% bridgmanite, 17 wt.% ferropericlase, and 7 wt.% calcium perovskite.

141 The ferropericlase, $(Mg_{0.85},Fe_{0.15})O$, hosts 15 mol% FeO^{30}. The Earth's actual mantle geotherm is

142 uncertain, and fitting PREM requires non-adiabatic gradients and/or variations in composition with

143 depth in the lower mantle[35]. Here the P-wave velocity in Fig. 1d is calculated using temperatures

144 that align pyrolite S-wave velocity to PREM[5] at each depth, thus highlighting the inability to

145 match both S-wave and P-wave constraints simultaneously when the effects of a spin crossover are

146 included (S-wave velocities are not significantly affected by the spin crossover, Fig. 2b).

Fast and slow mapping With the rapid development of data acquisition and improvements in inversion and modelling techniques in recent decades, numerous global seismic tomographic models are now available[36,37]. Most models agree on the large-wavelength structure of seismic velocity anomalies in the mantle. However, the amplitudes of the anomalies, as well as smaller scale-features such as individual subducted slabs, sometimes vary owing to differences in parameterization, data processing, regularization, and other subjective influences[18]. There are also few joint P- and S-wave models that do not include some type of scaling of the P-wave model to the S-wave model in the lower mantle.

Instead of solely relying on particular P- and S-wave model pairs, we set a uniform grid in the mantle and tabulated the number of models ("votes") that reveal a $>1\sigma$ (i.e., equal to or greater than one standard deviation from the mean) seismic velocity anomaly at each location[20]. Vote maps are a simple tool, developed to detect the existence and distribution of material with particular seismic characteristics in the lower mantle, and are ideal for probing signals within seismically fast (e.g. $+1\sigma$; mainly slabs - Fig. 1b,3,4) and slow (-1σ; plumes, LLSVPs - Fig. 1c,3,4) mantle regions. For example, the pattern of fast anomaly vote maps (Fig. 3) reveals N-S trending slabs under North America, related to long-lived subduction along eastern Panthalassa, as well E-W trending slabs related to palaeo-subduction within the Tethys Ocean[20]. We use the standard deviation instead of choosing particular seismic velocity amplitudes because the latter vary significantly between different models and reflect subjective choices in model construction (such as regularization) and the quantity of seismic data employed in the inversion[38].

9

167 The models were chosen to capture a variety of data types and processing techniques that

168 are employed in tomographic inversions. The 4 P-wave models are DETOX-P01[39], GAP-P4[40,41],

169 HMSL-P06[19], MITP-2011[42], and the 4 S-wave models are HMSL-S06[19], S40RTS[43], savani[44],

170 SEMUCB-WM1[45]. These models are not filtered to exclude any spherical harmonic degrees. All

171 of these models can be accessed via the SubMachine website[46] http://submachine.earth.ox.ac.uk/.

172 As outlined in the original vote map methodology[20], the individual tomography models are linearly

173 interpolated along a 0.5° grid with a depth increment of 50 km. Processing was done with Generic

174 Mapping Tools (GMT, version 5.3.1[47]). The vote map methodology uses sigma values (standard

175 deviation) as the contour metric for each tomography model at each depth (i.e.[38]). Each model

176 contributes one vote at each grid cell according to whether the model value lies inside (vote=1) or

177 outside (vote=0) the specified contour (as inspired by cluster analysis of [48]). Extended Data. Fig.

178 4 shows an example of the vote map procedure. Votes for each of the 4 models are tabulated to

179 generate the final vote map grid. The resulting abundance profiles (in % of area) of agreement (i.e.

180 how many models agree at a given depth, where 4 votes is the maximum agreement) for alternative

181 sigma thresholds for the individual seismic tomography models is shown Extended Data. Figs.

182 1-2. Two additional tomography models TX2019[49] and SP12RTS[50] are included for comparison

183 (Extended Data. Fig. 3). Difference maps generated by subtracting the S-wave model votes from

184 the P-wave model votes are shown in Extended Data. Fig. 5. Scientific and perceptually uniform

185 colour maps from [51] were used in all figures.

186 **Data Availability** The datasets generated and/or analysed during the current study are available at

187 Zenodo [will be updated upon acceptance], temporary file link:

2 References

1. Badro, J. *et al.* Iron partitioning in Earth's mantle: Toward a deep lower mantle discontinuity. *Science* **300**, 789–791 (2003).

2. Tsuchiya, T., Wentzcovitch, R. M., da Silva, C. R. S. & de Gironcoli, S. Spin transition in magnesiowüstite in Earth's lower mantle. *Phys. Rev. Lett.* **96**, 198501 (2006).

3. Wu, Z., Justo, J. & Wentzcovitch, R. Elastic anomalies in a spin-crossover system: Ferroperi- clase at lower mantle conditions. *Phys. Rev. Lett.* **110**, 228501 (2013).

4. Lin, J.-F., Speziale, S., Mao, Z. & Marquardt, H. Effects of the electronic spin transitions of iron in lower mantle minerals: Implications for deep mantle geophysics and geochemistry. *Reviews of Geophysics* **51**, 244–275 (2013).

5. Dziewonski, A. & Anderson, D. Preliminary reference Earth model. *Phys. Earth Planet. Inter.* **25**, 297–356 (1981).

6. Stixrude, L. & Lithgow-Bertelloni, C. Geophysics of chemical heterogeneity in the mantle. *Ann. Rev. Earth Planet. Sci.* **40**, 569–595 (2012).

7. Wu, Z. & Wentzcovitch, R. Spin crossover in ferropericlase and velocity heterogeneities in the lower mantle. *Proc. Nat. Acad. Sci.* **111**, 10468–10472 (2014).

8. Wentzcovitch, R. *et al.* Anomalous compressibility of ferropericlase throughout the iron spin crossover. *Proc. Natl. Acad. Sc. USA* **106**, 8447–8452 (2009).

9. Mora, S. D., Boschi, L., Tackley, P. J., Nakagawa, T. & Giardini, D. Low seismic resolution cannot explain S/P decorrelation in the lower mantle. *Geophys. Res. Lett.* **38**, L12303 (2011).

10. Fei, Y. *et al.* Spin transition and equations of state of (Mg,Fe)O solid solutions. *Geophys. Res. Lett.* **34**, L17307 (2007).

11. Komabayashi, T., Hirose, K., Nagaya, Y., Sugimura, E. & Ohishi, Y. High-temperature compression of ferropericlase and the effect of temperature on iron spin transition. *Earth Planet. Sci. Lett.* **297**, 691–699 (2010).

12. Wu, Z. & Wentzcovitch, R. Composition versus temperature induced velocity heterogeneities in a pyrolitic lower mantle. *Earth Planet. Sci. Lett.* **457**, 359–365 (2017).

13. Marquardt, H. *et al.* Elastic softening of $(Mg_{0.8}Fe_{0.2})O$ ferropericlase across the iron spin crossover measured at seismic frequencies. *Geophys. Res. Lett.* **45**, 6862–6868 (2018).

14. Grand, S. Mantle shear-wave tomography and the fate of subducted slabs. *Phil. Trans. R. Soc. Lond. A* **360**, 2475–2491 (2002).

15. Ishii, M. & Tromp, J. Normal-mode and free-air gravity constraints on lateral variations in velocity and density of earth's mantle. *Science* **285**, 1231–1236 (1999). URL `https://science.sciencemag.org/content/285/5431/1231`. `https://science.sciencemag.org/content/285/5431/1231.full.pdf`.

16. Moulik, P. & Ekstrom, G. The relationships between large-scale variations in shear velocity, density, and compressional velocity in the Earth's mantle. *J. Geophys. Res.* **121**, 2327–2771 (2016).

17. Saltzer, R. L., van der Hilst, R. D. & Karason, H. Comparing P and S wave heterogeneity in the mantle. *Geophys. Res. Lett.* **28**, 1335–1338 (2001).

18. Houser, C. & Williams, Q. The relative wavelengths of fast and slow velocity anomalies in the lower mantle: Contrary to the expectations of dynamics? *Phys. Earth Planet. Int.* **176**, 187–197 (2009).

19. Houser, C., Masters, G., Shearer, P. & Laske, G. Shear and compressional velocity models of the mantle from cluster analysis of long-period waveforms. *Geophys. J. Int.* **174**, 195–212 (2008).

20. Shephard, G., Matthews, K., Hosseini, K. & Domeier, M. On the consistency of seismically imaged lower mantle slabs. *Science Reports* **7: 10976** (2017).

21. Iitaka, T., Hirose, K., Kawamura, K. & Murakami, M. The elasticity of the MgSiO3 post-perovskite phase in the Earth's lowermost mantle. *Nature* **430**, 442–445 (2004).

22. Wentzcovitch, R. M., Tsuchiya, T. & Tsuchiya, J. MgSiO3 postperovskite at D" conditions. *Proc. Nat. Acad. Sci.* **103(3)**, 543–546 (2006).

23. Hutko, A., Lay, T., Revenaugh, J. & Garnero, E. Anticorrelated seismic velocity anomalies from post-perovskite in the lowermost mantle. *Science* **320**, 1070–1074 (2008).

24. Garnero, E., McNamara, A. & Shim, S.-J. Continent-sized anomalous zones with low seismic velocity at the base of Earth's mantle. *Nature Geoscience* **9**, 481–489 (2016).

25. Piet, H. *et al.* Spin and valence dependence of iron partitioning in Earth's deep mantle. *Proc. Nat. Acad. Sci.* **113 (40)**, 11,127–11,130 (2016).

26. Persson, K., Bengtson, A., Ceder, G. & Morgan, D. Ab initio study of the composition dependence of the pressure-induced spin transition in the $(Mg_{1-x},Fe_x)O$ system. *Geophys. Res. Lett.* **33**, L16306 (2006).

27. Grand, S., van der Hilst, R. & Widiyantoro, S. Global seismic tomography: A snapshot of convection in the Earth. *GSA Today* **7**, 1–7 (1997).

28. Kellogg, L. & Turcotte, D. Mixing and the distribution of heterogeneities in a chaotically convecting mantle. *J. Geophys. Res.* **95**, 421–432 (1990).

29. Ballmer, M., Houser, C., Hernlund, J., Wentzcovitch, R. & Hirose, K. Persistence of strong silica-enriched domains in the Earth's lower mantle. *Nature Geoscience* **10**, 236–240 (2017).

30. Valencia-Cardona, J. *et al.* Influence of the iron spin crossover in ferropericlase on the lower mantle geotherm. *Geophys. Res. Lett.* **44**, 4863–4871 (2017).

31. Shukla, G. *et al.* Thermoelasticity of Fe^{2+}-bearing bridgmanite. *Geophys. Res. Lett.* **42**, 1741–1749 (2015).

32. Shukla, G., Cococcioni, M. & Wentzcovitch, R. Thermoelasticity of Fe^{3+}- and Al-bearing bridgmanite: Effects of iron spin crossover. *Geophys. Res. Lett.* **43**, 5661–5670 (2016).

33. Kulik, H. J., Cococcioni, M., Scherlis, D. A., & Marzari, N. Density functional theory in transition-metal chemistry: A self-consistent Hubbard U approach. *Physical Review Letters* **97** (2006).

34. McDonough, W. F. & Sun, S. The composition of the Earth. *Chemical Geology* **120**, 223–253 (1995).

35. Cobden, L. *et al.* Thermochemical interpretation of 1-D seismic data for the lower mantle: The significance of nonadiabatic thermal gradients and compositional heterogeneity. *J. Geophys. Res.* **114**, doi:10.1029/2008JB006262 (2009).

36. van der Hilst, R., Widiyantoro, S. & Engdahl, E. Evidence for deep mantle circulation from global tomography. *Nature* **386**, 578–584 (1997).

37. Simmons, N. A., Myers, S. C., Johannesson, G. & Matzel, E. LLNL-G3Dv3: Global P wave tomography model for improved regional and teleseismic travel time prediction. *J. Geophys. Res.* **117** (2012).

38. Hernlund, J. & Houser, C. On the distribution of seismic velocities in Earth's deep mantle. *Earth Planet. Sci. Lett.* **265**, 423–437 (2008).

39. Hosseini, K. & Sigloch, K. Multifrequency measurements of core-diffracted P waves (Pdiff) for global waveform tomography. *Geophys. J. Int.* **203**, 506–521 (2015).

40. Obayashi, M. *et al.* Finite frequency whole mantle P wave tomography: Improvement of subducted slab images. *Geophys. Res. Lett.* **40**, 5652–5657 (2013).

41. Fukao, Y. & Obayashi, M. Subducted slabs stagnant above, penetrating through, and trapped below the 660 km discontinuity. *J. Geophys. Res.* **118**, 5920–5938 (2013).

42. Burdick, S. *et al.* Model update March 2011: Upper mantle heterogeneity beneath North America from traveltime tomography with global and USArray Transportable Array data. *Seismological Research Letters* **83**, 23–28 (2012).

43. Ritsema, J., Deuss, A., van Heijst, H. J. & Woodhouse, J. H. S40RTS: A degree-40 shear-velocity model for the mantle from new Rayleigh wave dispersion, teleseismic traveltime and normal-mode splitting function measurements. *Geophys. J. Int.* **184**, 1223–1236 (2011).

44. Auer, L., Boschi, L., Becker, T. W., Nissen-Meyer, T. & Giardini, D. Savani: A variable resolution whole-mantle model of anisotropic shear velocity variations based on multiple data sets. *J. Geophys. Res.* **119**, 3006–3034 (2014).

45. French, S. W. & Romanowicz, B. A. Whole-mantle radially anisotropic shear velocity structure from spectral-element waveform tomography. *Geophys. J. Int.* **199**, 1303–1327 (2014).

46. Hosseini, K. *et al.* Submachine: Web-based tools for exploring seismic tomography and other models of Earth's deep interior. *Geochem. Geophys. Geosys.* **19**, 1464–1483 (2018).

47. Wessel, P., Smith, W., Scharroo, R., Luis, J. & Wobbe, F. Generic Mapping Tools: Improved Version Released. *EOS Transactions* **94**, 409–420 (2013).

48. Lekic, V., Cottaar, S., Dziewonski, A. & Romanowicz, B. Cluster analysis of global lower mantle tomography: A new class of structure and implications for chemical heterogeneity. *Earth Planet. Sci. Lett.* **357358**, 6877 (2012).

49. Lu, C., Grand, S. P., Lai, H. & Garnero, E. J. TX2019slab: A new P and S tomography model incorporating subducting slabs. *Journal of Geophysical Research: Solid Earth* **124**, 11549–11567 (2019).

50. Koelemeijer, P., Ritsema, J., Deuss, A. & van Heijst, H.-J. SP12RTS: A degree-12 model of shear- and compressional-wave velocity for Earth's mantle. *Geophysical Journal International* **204**, 1024–1039 (2016).

51. Crameri, F. Geodynamic diagnostics, scientific visualisation and StagLab 3.0. *Geosci. Model Dev.* **11**, 2541–2562 (2018).

52. Mueller, R. D. *et al.* Ocean basin evolution and global-scale plate reorganization events since pangea breakup. *Annual Review of Earth and Planetary Sciences* **44**, 107–138 (2016).

Correspondence   Correspondence and requests should be addressed to G.E.S: grace.shephard@geo.uio.no

Figure 1 Comparison of mineral physics predictions and seismological observations of

the Fe spin crossover in Fp. (a) the pressure/depth-temperature distribution of low-spin

Fe and three schematic mantle geotherms. The onset of the mixed spin region occurs

at shallower depths for relatively colder temperatures and at greater depths and over a

broader range at higher temperatures. Profiles of vote map area coverage of unanimous

consensus (4/4 models) for a velocity anomaly (corresponding to the vote maps shown

in Figures 3 and 4) for fast (b) and slow (c) mantle. A drop in the coherent seismic

signal between P-wave models relative to S-wave models is revealed below the respective

"onset" depths of approximately 1,400 km and 1,800 km. (d) The predicted[30] profile of P-

wave velocities for pyrolite using temperatures that fit S-wave velocities to PREM[5] reveals

a significant departure suggesting that the signature of the spin transition is not a globally-

averaged feature. See Methods.

Figure 2 Depth/pressure dependence of elastic moduli and of seismic velocities for

pyrolite[34] containing 17 wt.% Fp with 15 mol% of FeO, 76 wt.% bridgmanite and 7 wt.%

of calcium perovskite[30]. (a) Shear and bulk moduli. The anomalous behaviour of the

bulk modulus, K,[8] ($K = -V(dP/dV)$, where V is volume and P is pressure) is due to

the iron octahedron volume collapse during the spin-state change[2] associated with the

spin crossover. As previously shown[8], the pressure onset, the pressure range of the

HS-LS crossover, and associated anomalies in K are temperature dependent (same leg-

end all panels). The shear modulus, G, ($G = \tau/\gamma$, where τ is the shear stress and γ

is the shear strain) is not significantly affected by the octahedron volume reduction and

increases monotonically with increasing pressure and decreasing temperature. (b) S-wave ($V_s = \sqrt{G/\rho}$) and (c) P-wave ($V_p = \sqrt{(K + 4/3G)/\rho}$) velocity for pyrolite at different temperatures. The average mantle temperature profile (black) is calculated by setting the starting temperature to 1873 K at 660 km, and integrating the adiabatic temperature gradient[30] through the lower mantle. The blue/magenta curves were calculated using the same technique, but decreasing/increasing the temperature at 1873 km by $\pm$500 K. In the mixed-spin region, the softening of K^8 causes a reduction in P-wave velocity sensitivity to isobaric temperature variations[7], while the S-wave velocity remains sensitive to such temperature variations. Consequently, the expected seismic signal of Fp in the lower mantle consists of a disruption of vertically coherent thermal structures in P-velocities, whereas a coherent thermal structure is apparent in the S-velocities[7,12]

Figure 3 Vote maps of mantle tomography models. Variable depth vote maps for fast ($>+1\sigma$ from the mean), and slow ($<-1\sigma$ from the mean) mantle for all (a) 4 S-wave and (b) 4 P-wave tomography models (see Methods) considered here. In general, fast maps reveal subducted slabs and slow maps reveal plumes and antipodal large low shear wave velocity provinces (LLSVPs). In this map view, the P-wave model vote maps appear less coherent than the S-wave model vote maps in the fast velocity regions of the mid-mantle. Colour maps from[51].

Figure 4 Vertical cross sections through the vote maps. All 4 S-wave models (left) and 4 P-wave models (right) are used for profiles through (a) SE Asia and (b) the Farallon slab

20

regions (fast vote maps), and (c) the African-Afar large low shear wave velocity province (LLSVP) and plume region (slow vote maps). Location maps are overlain with palaeo-subduction zones between 0-200 Ma as extracted from a global plate reconstruction[52]. Panels (a) and (b) identify fast regions that are coherent between S-wave models but lose coherency in the mid-mantle amongst P-wave models. This is more clear in the fast rather than (c) slow regions because at higher temperatures the HS-LS crossover shifts to depths at the base of the mantle where the seismic signal is dominated by the LLSVPs.

FIGURE 1

FIGURE 2

FIGURE 3

a. S-wave tomography models

Fast anomalies (>+1σ)   Slow anomalies (<-1σ)

b. P-wave tomography models

Fast anomalies (>+1σ)   Slow anomalies (<-1σ)

1000 km

1400 km

2000 km

2400 km

2800 km

0   1   2   3   4
Number of models

0   1   2   3   4
Number of models
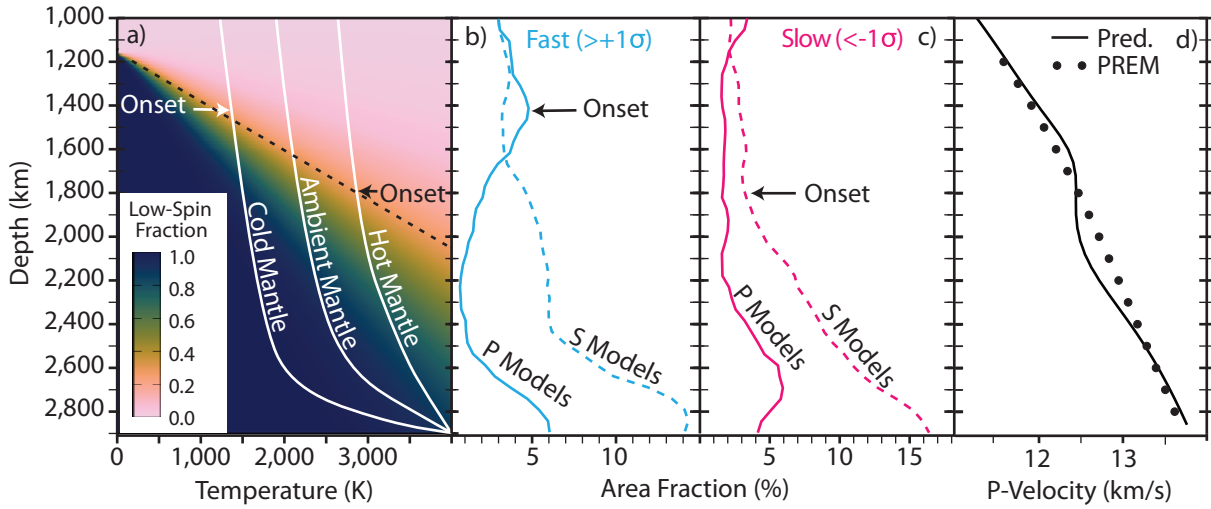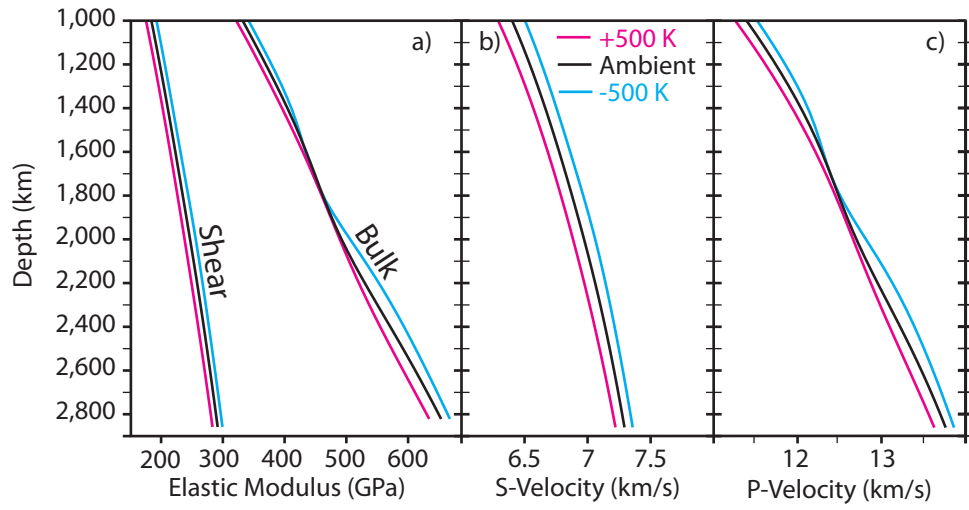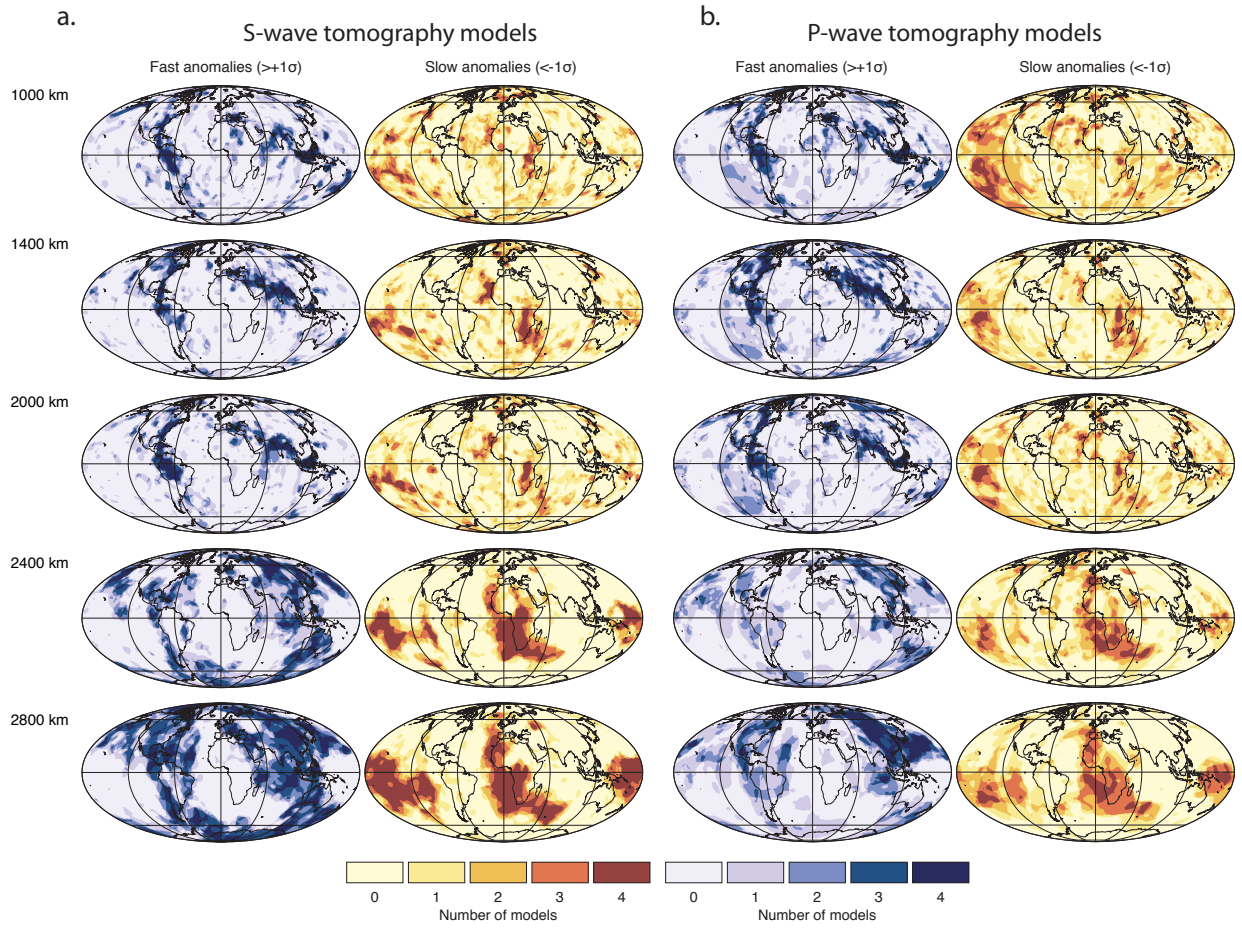
FIGURE 4
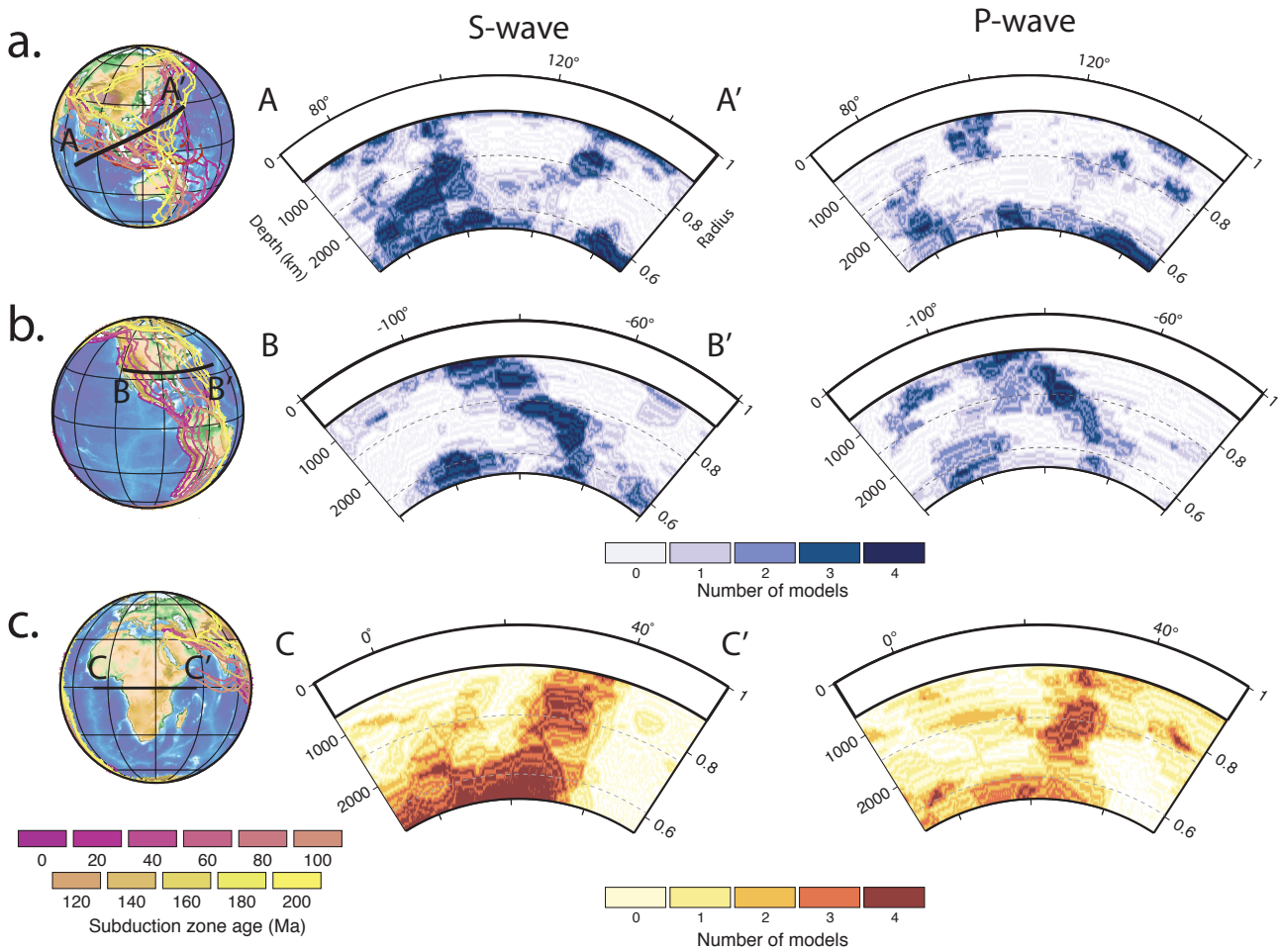
Extended Data: Seismological Expression of the Iron Spin Crossover in Ferropericlase in the Earth's Lower Mantle

Grace E. Shephard*[1], Christine Houser[2], John W. Hernlund[2], Juan J. Valencia-Cardona[3],

Reidar G. Trønnes 1,4 Renata M. Wentzkovitch 2, 5, 6

1 Center for Earth Evolution and Dynamics (CEED), Department of Geosciences, University of

Oslo, Norway **2** Earth-Life Science Institute, Tokyo Institute of Technology, Tokyo, Japan **3** Department of Chemical Engineering and Material Science, University of Minnesota, Twin Cities,

USA   4 Natural History Museum, University of Oslo, Norway 5 Department of Earth and

Environmental Sciences, Columbia University, Lamont-Doherty Earth Observatory, Palisades,

USA 6 Department of Applied Physics and Applied Mathematics, Columbia University,

New York City, USA

Supplementary Figures

Extended Data Figure 1 Area fraction of fast ($>+0.75$, $>+1$, $>+1.25$ σ) anomalies as a

function of depth for the 8 tomography models. This is similar to Fig. 1b (and Extended Data

Fig. 3 for HMSL[1]), but presented here for the individual tomography models (4 P-wave and 4

S-wave) prior to being summed into the vote map. There is high variability between and within the

individual tomography models, including the joint HMSL models. While a decorrelation between

P- and S-wave models is apparent between some model combinations, it is not in others, which

is why a single pair of tomography models in isolation does not render a robust signal of the spin

1

transition.

Extended Data Figure 2 Area fractions of slow ($<$-0.75, $<$-1, $<$-1.25 σ) anomalies as a function of depth for the 8 tomography models. Similar to Fig. 1c, but here presented for the individual tomography models (4 P-wave and 4 S-wave) prior to being summed into the vote map. As with the fast anomalies (Extended Data Figure 1) there is high variability between the models.

Extended Data Figure 3 Area coverage as a function of depth for different combinations of the 4 seismic tomography models for each of the P-wave models and S-wave models. Top panels: fast anomalies, bottom panels: slow anomalies. This is similar to Fig. 1b-c, but with different tomography models being added sequentially (listed within the panels). In addition to the 8 models used in the paper, the joint tomography models of SP12RTS[2] and TX2019[3] are also included for reference. The trend between P- and S-wave models is somewhat variable between the individual model pairs of SP12RTS, TX2019, and HMSL but do hint at a mid-mantle decorrelation related to the spin crossover (see also Extended Data Figures 1-2). However, the signal becomes more apparent when the models are summed into the vote maps, which identify the most common features between tomography models.

Extended Data Figure 4 An example figure of the vote map procedure for fast anomalies at 1000 km depth before the models are added into vote maps. Shephard et al. (2017)[4] presents further details of the vote map methodology. Each of the 8 tomography models are shown in their original format (panel a) and after the gaussian fitting (panel b). The models are contoured for values equal to or higher than +0.75, +1, +1.25 σ) anomalies for the P-wave models (panels c, d, e)

and S-wave models (panels f, g, h), respectively. The fast vote maps in the main manuscript were constructed from the $>+1$ sigma vote maps.

Extended Data Figure 5 Difference maps for the fast (left panels) and slow (right panels) vote maps constructed by subtracting the S-wave model votes (constructed with 4 models) from P-wave model votes (constructed with 4 models). Blue areas indicate high votes (i.e. the identification of robust features) in P-wave models but not S-wave models, red areas indicate high votes for S-wave models relative to P-wave models, and central colours indicate regions of mutual agreement.

Extended Data Figure 6 The self-consistent geotherms for pyrolite calculated by setting the starting temperature of the calculation at the top of the lower mantle to 1373 K (blue, the -500 K case), 1873 K (black, the average case), and 2373 K (red, the +500 K case) for the elastic moduli and velocity profiles plotted in Figure 2.

Extended Data Figure 7 The change in the seismic velocities using constant versus depth-dependent partitioning of iron between Br and Fp, K_D. Panel (a): Depth-dependent K_D[5] curve (dashed line) and the constant 0.5 value (solid line) used in the main text. Panels (b and c): Shear and compressional velocities for the depth-dependent K_D[5] case (dashed lines) and the constant value 0.5 case (solid lines, same as Figure 2). A higher proportion of Fe in the ferropericlase (lower K_D) may increase the crossover pressure[6]. We find that Fe in ferropericlase remains below the 25% threshold for observing substantial increases in the crossover transition pressure[7] for the depth-dependent K_D case. Thus, depth-dependent K_D does not have a significant influence on

the crossover depth/pressure range over which we observe the anomalous signal in compressional velocity in the tomographic models.

1. Houser, C., Masters, G., Shearer, P. & Laske, G. Shear and compressional velocity models of the mantle from cluster analysis of long-period waveforms. *Geophys. J. Int.* **174**, 195–212 (2008).

2. Koelemeijer, P., Ritsema, J., Deuss, A. & van Heijst, H.-J. SP12RTS: A degree-12 model of shear- and compressional-wave velocity for Earth's mantle. *Geophysical Journal International* **204**, 1024–1039 (2016).

3. Lu, C., Grand, S. P., Lai, H. & Garnero, E. J. TX2019slab: A new P and S tomography model incorporating subducting slabs. *Journal of Geophysical Research: Solid Earth* **124**, 11549–11567 (2019).

4. Shephard, G., Matthews, K., Hosseini, K. & Domeier, M. On the consistency of seismically imaged lower mantle slabs. *Science Reports* **7: 10976** (2017).

5. Piet, H. *et al.* Spin and valence dependence of iron partitioning in Earth's deep mantle. *Proc. Nat. Acad. Sci.* **113 (40)**, 11,127–11,130 (2016).

6. Lin, J.-F., Speziale, S., Mao, Z. & Marquardt, H. Effects of the electronic spin transitions of iron in lower mantle minerals: Implications for deep mantle geophysics and geochemistry. *Reviews of Geophysics* **51**, 244–275 (2013).

7. Persson, K., Bengtson, A., Ceder, G. & Morgan, D. Ab initio study of the composition dependence of the pressure-induced spin transition in the $(Mg_{1-x}, Fe_x)O$ system. *Geophys. Res. Lett.* **33**, L16306 (2006).

EXTENDED DATA FIGURE 1

P-wave tomography models (fast anomalies)

S-wave tomography models (fast anomalies)

EXTENDED DATA FIGURE 2
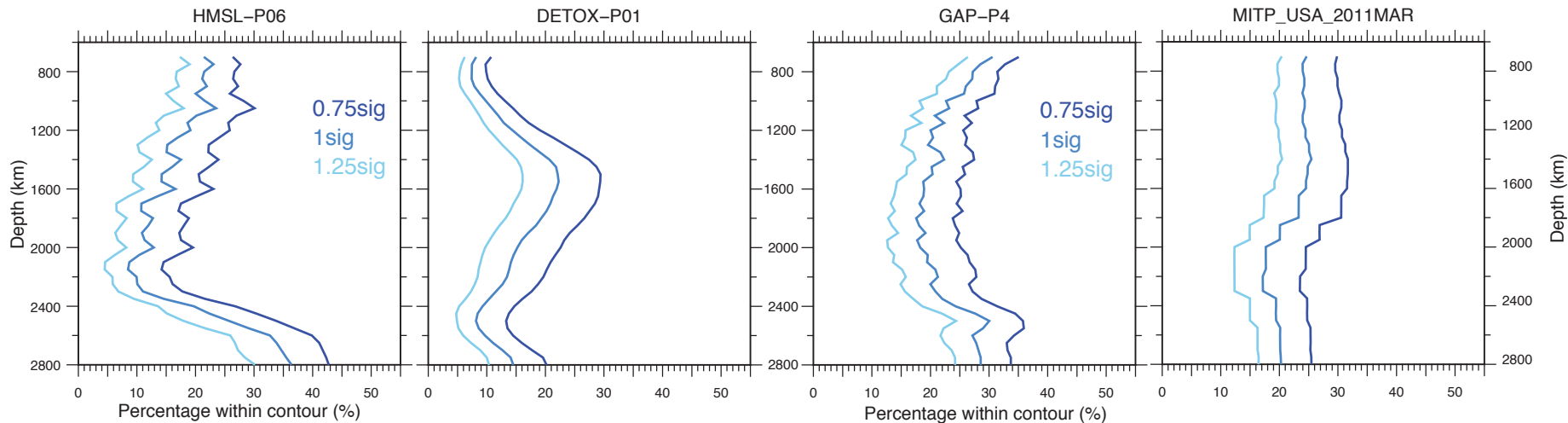
P-wave tomography models (slow anomalies)
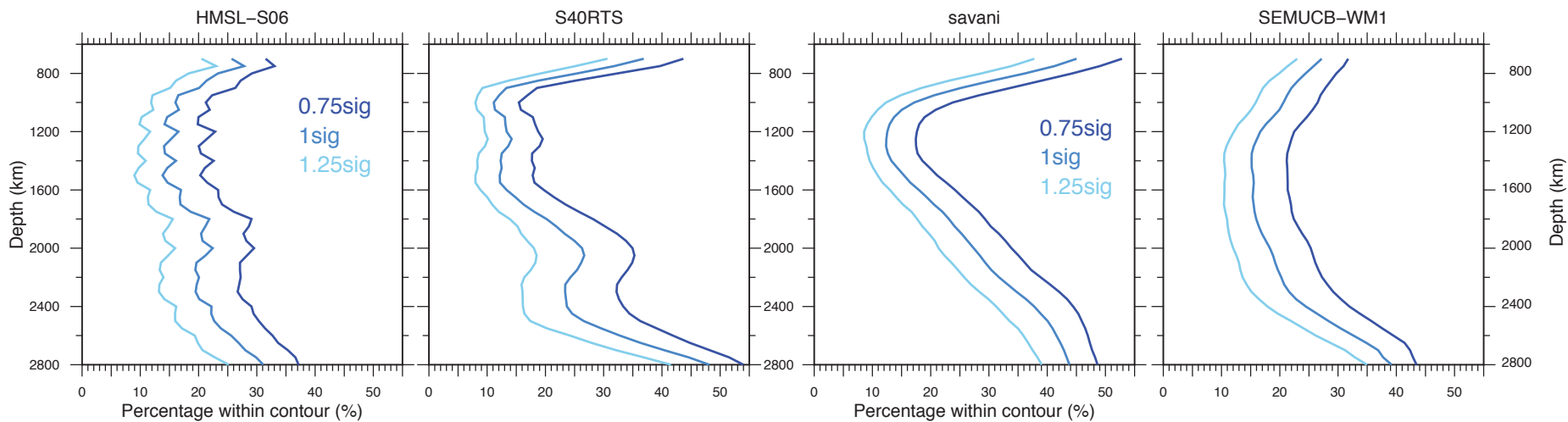
S-wave tomography models (slow anomalies)
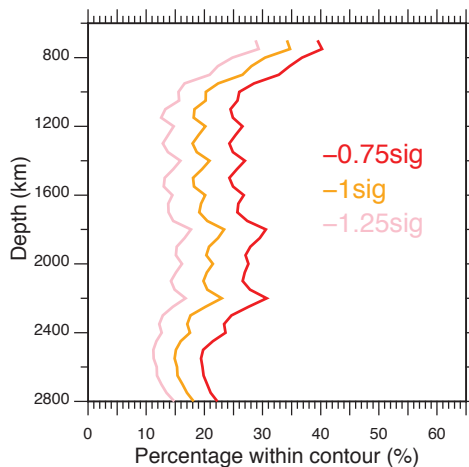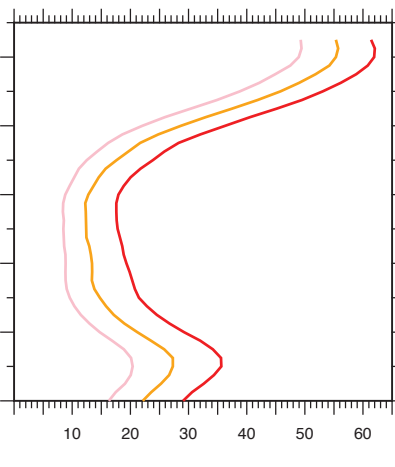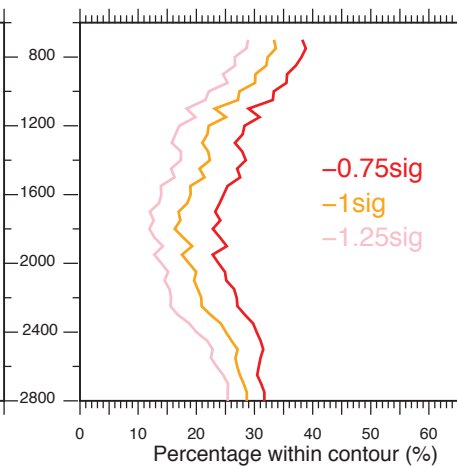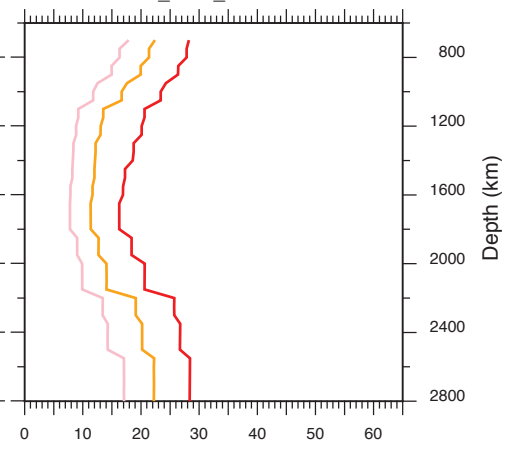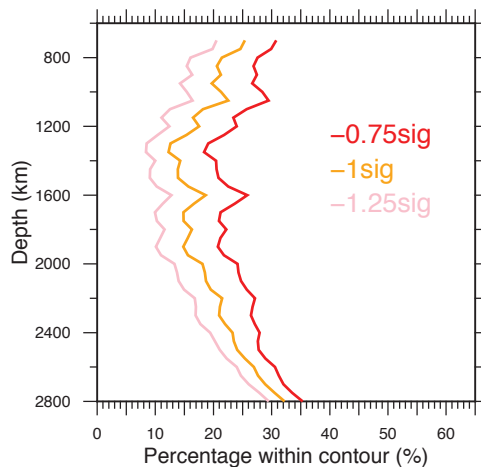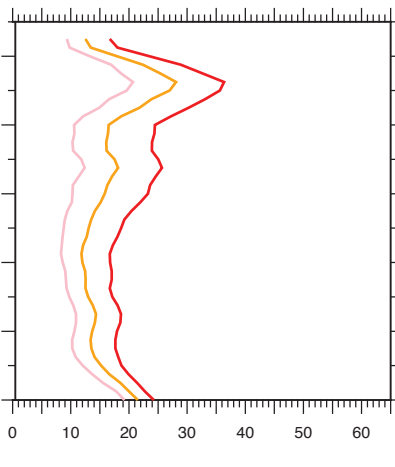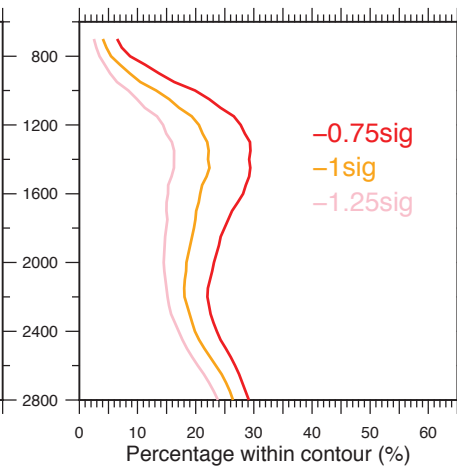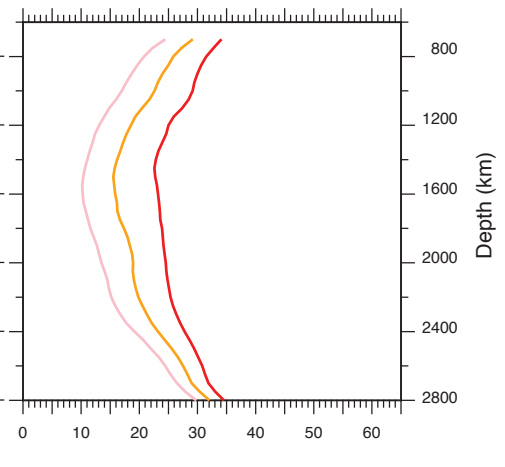
EXTENDED DATA FIGURE 3
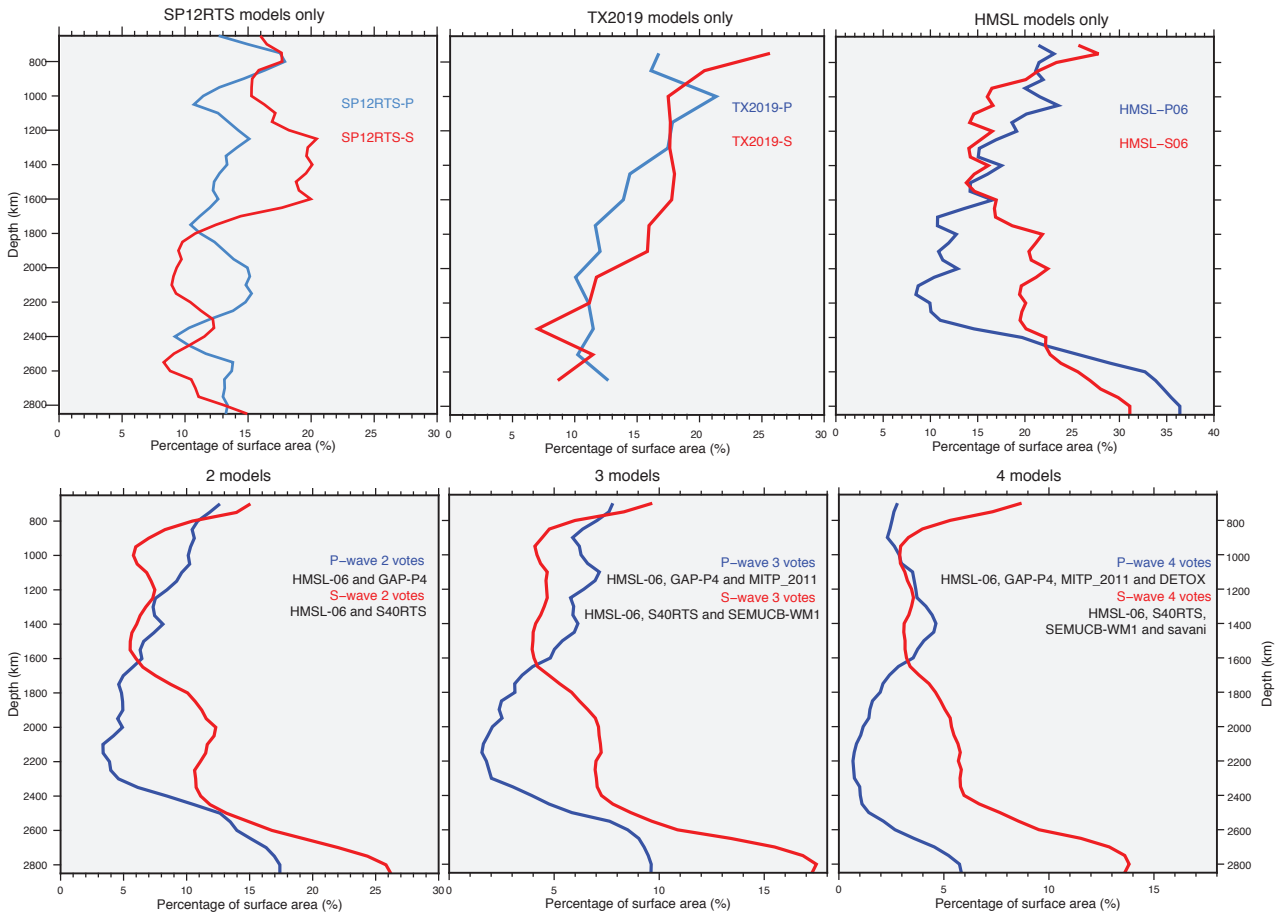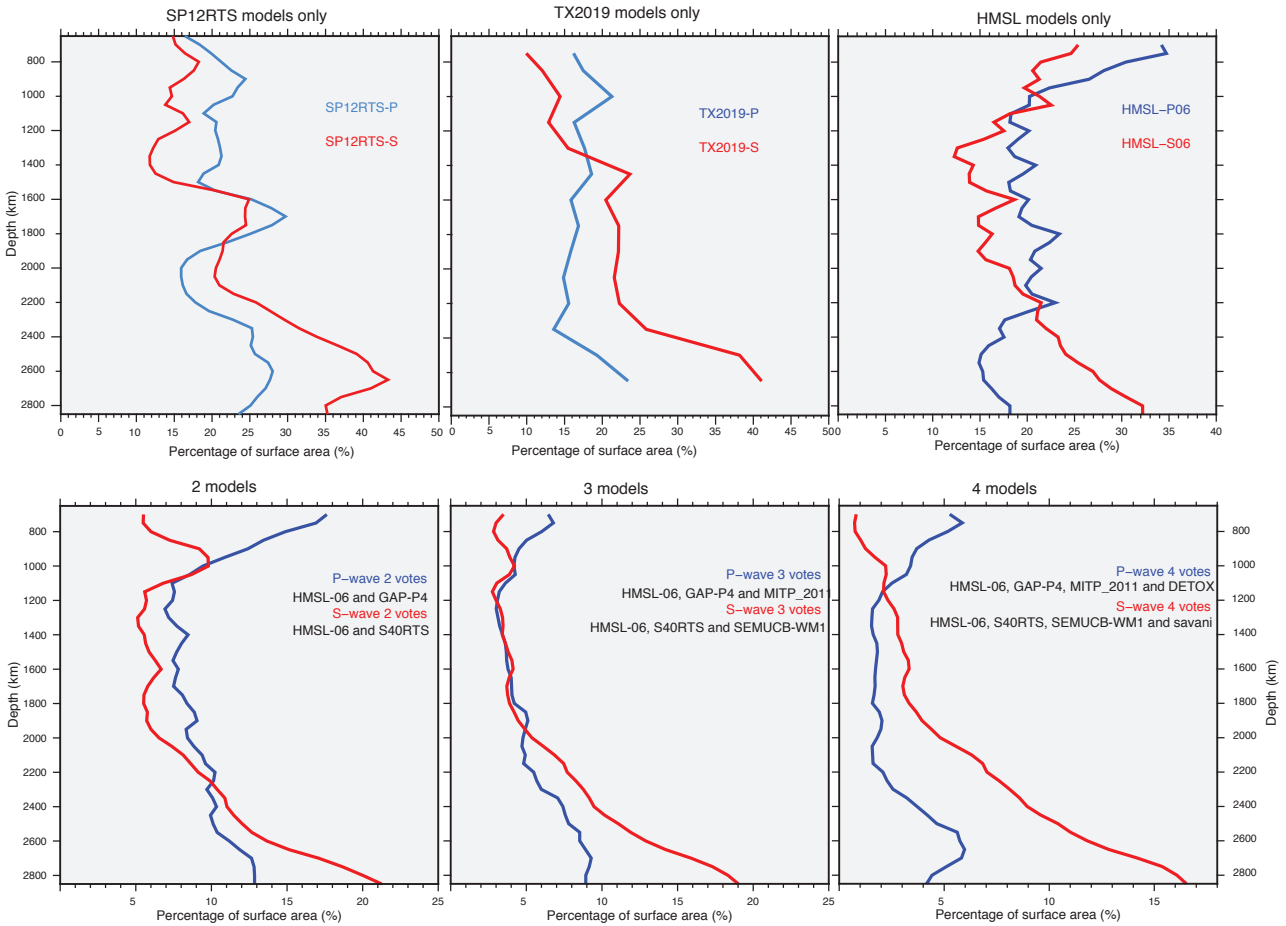
Fast anomalies at 1000 km depth
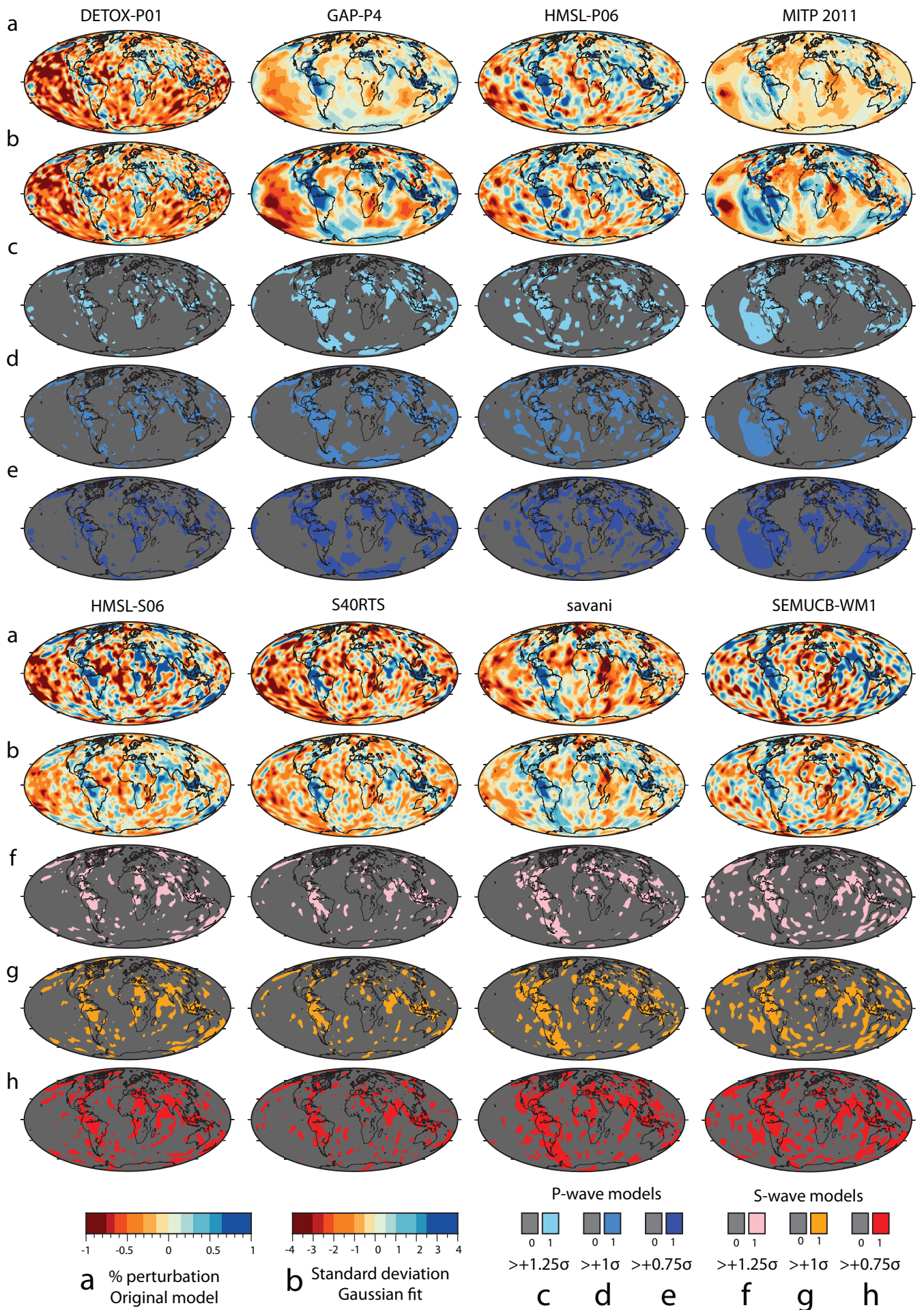
Difference (P-wave minus S-wave votes)
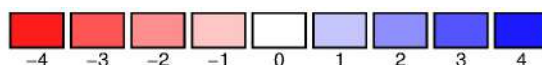
Fast anomalies (>+1σ)　　　　　Slow anomalies (<-1σ)
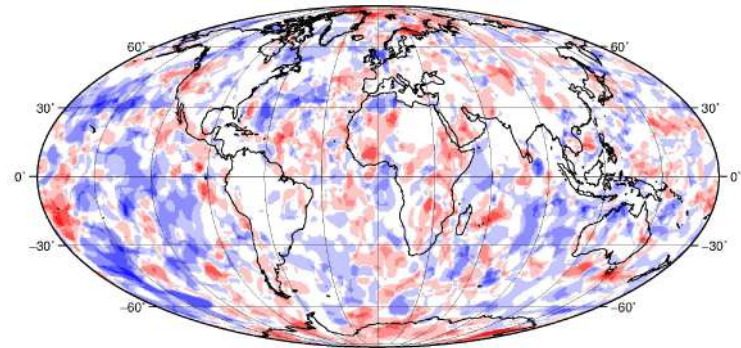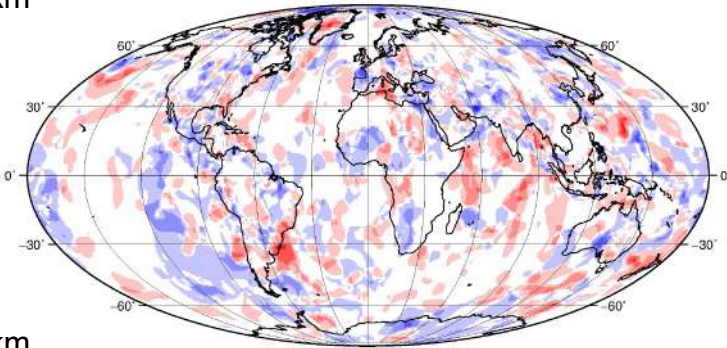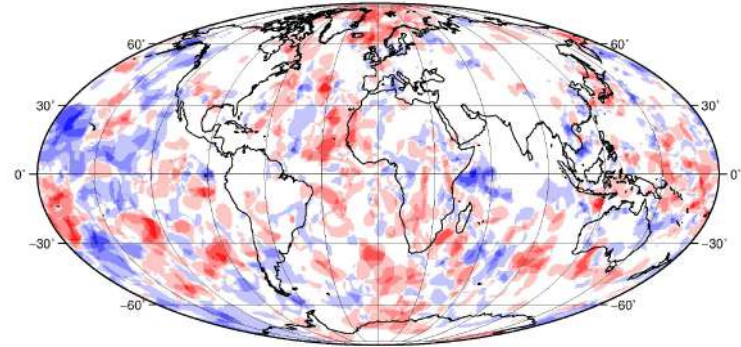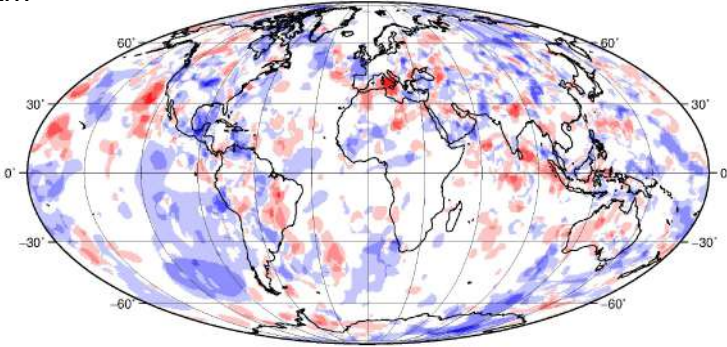
1000 km

1400 km

2000 km
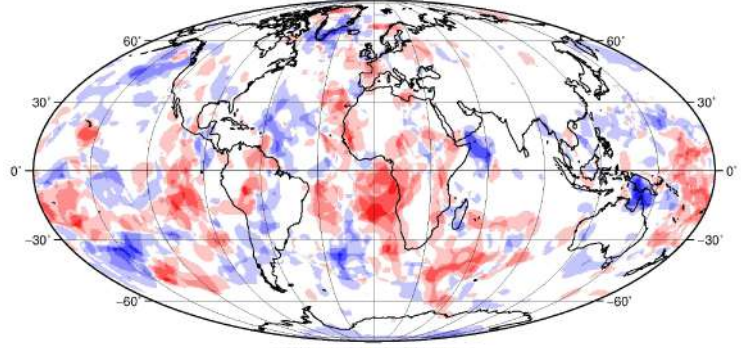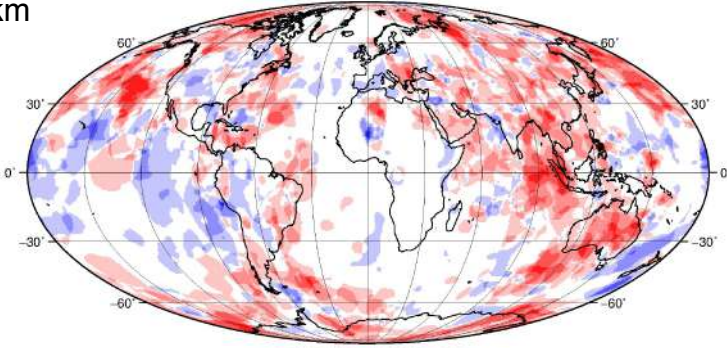
2400 km
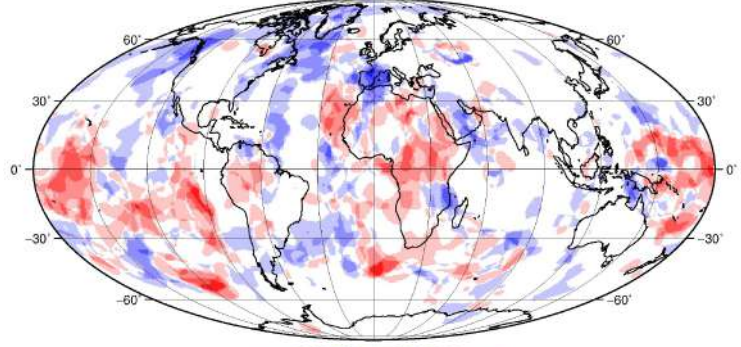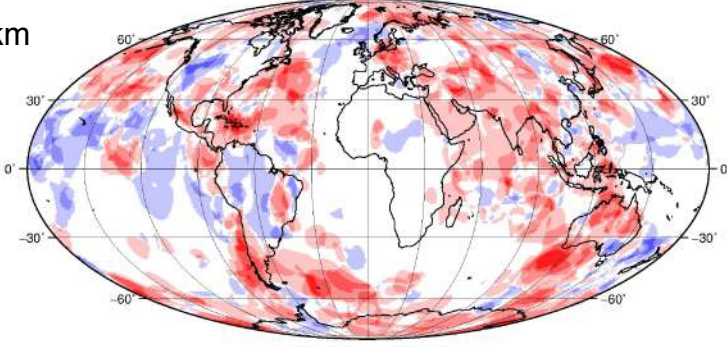
2800 km
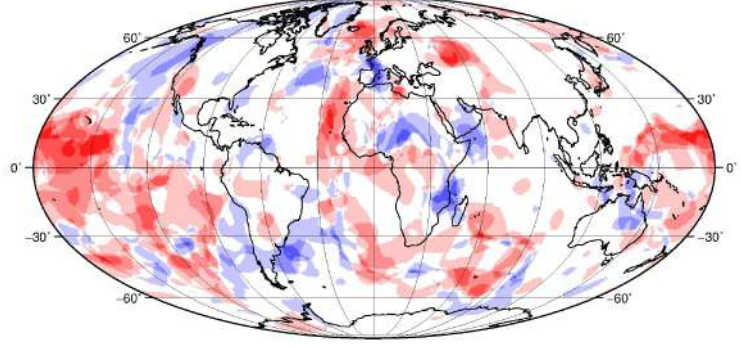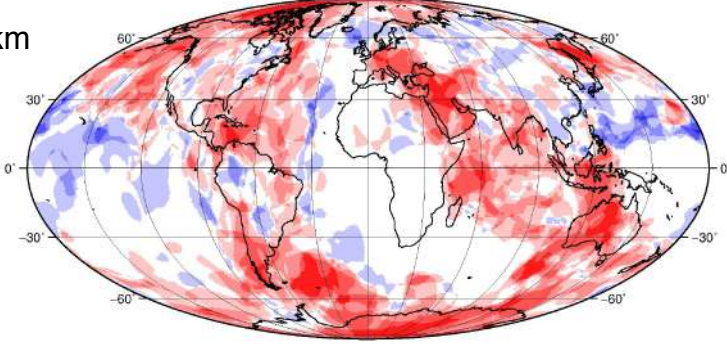
Number of votes (Vp minus Vs)

−4　−3　−2　−1　0　1　2　3　4

EXTENDED DATA FIGURE 7